Materials Advances

ROYAL SOCIETY OF CHEMISTRY

PAPER

View Article Online
View Journal | View Issue

Cite this: *Mater. Adv.*, 2021, 2, 4643

2,2′-(Arylenedivinylene)bis-8-hydroxyquinolines exhibiting aromatic π–π stacking interactions as solution-processable p-type organic semiconductors for high-performance organic field effect transistors†

Suman Sehlangia,[a] Shivani Sharma,[b] Satinder K. Sharma*[b] and Chullikkattil P. Pradeep *[a]

Solution-processable organic semiconductors capable of functioning at low operating voltages (~5 V) are in demand for organic field-effect transistor (OFET) applications. Exploration of new classes of compounds as organic thin-film transistor (OTFT) materials is an emerging research area. In this paper, a new series of π-conjugated oligomeric compounds, 2,2′-(arylenedivinylene)bis-8-hydroxyquinolines, has been explored as solution-processable organic semiconductor materials for low voltage OFET application for the first time. Crystal structure as well as Hirshfeld surface analyses of one of the compounds revealed the existence of strong face-to-face π–π stacking interactions among the molecules leading to the infinite chain-like arrangements in the crystal lattice. These π–π stacking interactions are further supported by several O–H···O, C–H···O and C–H···S interactions as well. In the slipped face-to-face π–π stacking interactions exhibited by these molecules, the inter-planar distances were in the range 3.491–3.5262 Å, while the slippage angles were in the range 18.8–20.4°. This class of compounds is soluble in common organic solvents such as tetrahydrofuran (THF), which ensures their solution processability. The semiconducting properties of these compounds were established by fabricating OFET structures using polymethylmethacrylate (PMMA) as the dielectric material. The transfer and output characteristics revealed p-type semiconducting behavior exhibiting considerable high field-effect hole mobilities of ~1.28 $cm^2 V^{-1} s^{-1}$ at low operating voltages (<6 V) and a considerable $I_{on/off}$ ratio of 10^3 at 75 °C. These results successfully demonstrated the potential candidature of 2,2′-(arylenedivinylene)bis-8-hydroxyquinoline derivatives for high-performance OFET applications.

Received 11th March 2021,
Accepted 1st June 2021

DOI: 10.1039/d1ma00215e

rsc.li/materials-advances

Introduction

Small-molecule organic semiconductors (SMOSCs) have gained attention in recent years because of their increasing utility in areas such as organic light-emitting diodes (OLEDs),[1] organic field-effect transistors (OFETs),[2] organic solar cells (OSCs)[3] and dye-sensitized solar cells (DSSCs).[4] In comparison to the traditional inorganic semiconducting materials, SMOSCs exhibit many desirable features including solution processability, high purity, low-temperature processability, flexible substrate printing, tuneable properties and so on.[5] One major area wherein SMOSCs find extensive application is OFETs. During the last decade, many studies have reported the development of new OFET materials as bio/chemical sensors, radio frequency identification components, organic active matrix displays, inverters, and logic circuits.[6,7] Despite the commendable progress achieved so far, there are still many open challenges to be addressed in the field of organic electronics. One such challenge is the poor carrier mobility of organic semiconductors in comparison to inorganic semiconductors.[8] A second challenge is the high operating voltage of OFETs, which leads to large power dissipation in the circuitry. Therefore, attaining high drain currents (I_{ds}) at relatively low operating voltages is extremely important for the practical applications of OFETs. A third challenge is the lack of sufficient knowledge about the structure–activity relationship of organic semiconductor materials. The structural and supramolecular analyses of organic semiconductors are

[a] *School of Basic Sciences, Indian Institute of Technology Mandi, Kamand-175 005, Himachal Pradesh, India. E-mail: pradeep@iitmandi.ac.in; Fax: +91 1905 267009; Tel: +91 1905 267045*

[b] *School of Computing and Electrical Engineering, Indian Institute of Technology Mandi, Kamand-175 005, Himachal Pradesh, India. E-mail: satinder@iitmandi.ac.in; Fax: +91 1905 267009; Tel: +91 1905 267134*

† Electronic supplementary information (ESI) available. CCDC 2065427. For ESI and crystallographic data in CIF or other electronic format see DOI: 10.1039/d1ma00215e

important for establishing a reliable structure–activity relationship.[9] It has been noted that the semiconducting properties of an organic conjugated molecule depends to a large extent on its intermolecular interactions and packing-order in solid-state.[10] Especially, the face-to-face π–π stacking interactions among the molecules are known to provide transport channels in SMOCs.[10,11] Therefore, there has been considerable interest in the development of new materials exhibiting excellent face-to-face π–π stacking interactions for SMOC applications in recent years.[12] In π–π stacked SMOCs, factors such as large π–π orbital overlap, short π–π distance, optimal π–π displacement, *etc.* are shown to enhance the charge transport properties.[13]

8-Hydroxyquinoline (8-HQ) is a heterocyclic moiety useful for diverse applications. Derivatives of 8-HQ are known to exhibit biological properties including antibacterial and anti-cancer activities.[14] 8-HQs are also important because of their unique coordination and photophysical properties.[15] For example, the excellent optical and chelating properties of 8-HQ have led to the development of tris(8-hydroxyquinolinato)aluminium(III), which is one of the most successful metal complexes reported so far for OLED applications.[16] Although 8-HQ derivatives have been widely explored for their photo-luminescence and biological applications, relatively few studies have been devoted to their semiconducting applications. A plausible explanation for this could be that a majority of the reported 8-HQ derivatives have a single 8-HQ unit per molecule and thus possess limited molecular conjugation. In 2005, Liang *et al* reported a series of π-conjugated oligomers bearing two 2-vinylene-8-substituted quinolines per molecule for photoluminescence and electroluminescence applications.[17] The applicability of 8-HQ derivatives in the development of hole-transport materials has been reported by Zeng *et al* in 2006.[18] However, reports on 8-HQ based extended π-conjugated systems for organic semiconductor applications are extremely rare and there is a huge potential in the development of such materials for diverse electronic applications.

Herein, we report two 8-HQ based π-conjugated oligomeric compounds, 2,2′-(arylenedivinylene)bis-8-hydroxyquinolines, **D1** and **D2**, as shown in Scheme 1(a), as p-type organic semiconductors exhibiting good hole mobility at relatively low operative voltages (<6 V). To understand the structure–activity relationship, the single crystal X-ray crystallography and Hirshfeld surface analyses of one of the compounds have been performed, which revealed strong face-to-face π–π stacking interactions among the molecules leading to the formation of π–π stacked 1-D infinite chains in the crystal lattice. The solution processability of these compounds permitted spin coating on large area substrates like indium tin oxide (ITO), which acts as a gate, along with PMMA as the dielectric material and silver as the source (S) and drain (D) electrodes for OFETs structures. The fabricated OFET devices were found to operate at relatively low operating voltages (<6 V) exhibiting high hole mobilities up to ~1.28 $cm^2 V^{-1} s^{-1}$. These preliminary studies, therefore, revealed the exciting potential of this class of compounds for commercial-scale organic semiconducting applications.

Results and discussion

The π-conjugated oligomeric compounds, **D1** and **D2**, were synthesized by reacting 8-hydroxyquinaldine with the corresponding dialdehydes in acetic anhydride under reflux conditions following a reported procedure.[19] **D1** and **D2** showed solubility in tetrahydrofuran (THF) and a few aprotic solvents.

Single crystals of **D1** suitable for crystallographic analyses were grown from methanol by the dichloromethane diffusion method. The crystals of **D2** grown under similar conditions were poorly diffracting and our repeated attempts to grow good quality crystals were unsuccessful. **D1** crystallized in monoclinic $P2_{1/c}$ space group having one molecule and one solvent water molecule in the asymmetric unit. The structure and refinement data of **D1** are given in Table S1 in the ESI† and the molecular structure showing atom labeling scheme is given in Fig. 1.

The molecule shows *E* conformation about both the styryl C=C bonds. The plane of the 8-HQ ring consisting of the atoms C10–C18 and N1 makes a dihedral angle of 31.23° with the plane of the central phenol ring (consisting of atoms C1–C6), while the second 8-HQ ring consisting of atoms C21–C29 and N2 makes a dihedral angle of 54.31° with the plane of the central phenol ring. This shows that the molecule is not planar and exhibits a twisted geometry, see Fig. 2. This contrasts with the similar compounds reported by Liang *et al.*,[17] in which the two quinolyl rings were more or less coplanar with the central aromatic ring. The bond distances C8–C9 and C19–C20 of the styryl moieties are 1.327(6) and 1.349(6) Å respectively,

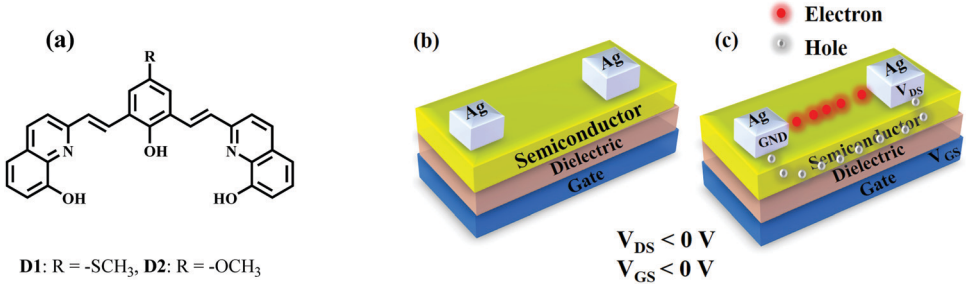

Scheme 1 (a) Chemical structure of the organic semiconducting materials **D1** and **D2**; (b) cross-section of OFETs based on **D1** and **D2** as the organic semiconductor layers in Bottom-Gate-Top-Contact structures: Ag(S&D)/**D1** or **D2**/PMMA/ITO; (c) at negative applied voltage, the accumulation of holes occurs for active transistor action.

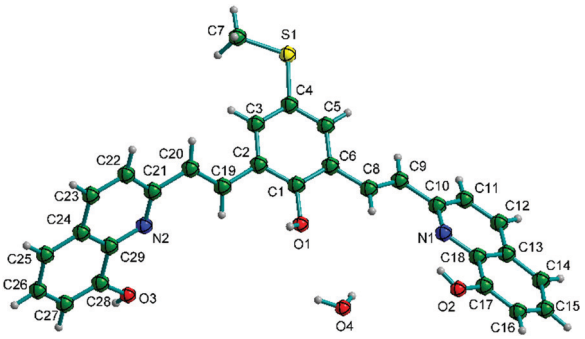

Fig. 1 Molecular structure of **D1** showing atom labeling scheme.

which are characteristic of the double bonds of alkenyl groups. The C6–C8, C9–C10, C2–C19 and C20–C21 bond lengths are 1.463(6), 1.478(6), 1.474(5) and 1.476(5) Å, respectively, which are slightly shorter than the standard C–C single bond length (*ca.* 1.5 Å) probably due to conjugation.

The two 8-HQ moieties of each molecule of **D1** make strong face-to-face π–π stacking interaction with similar moieties of the adjacent molecules as shown in Fig. 2. The π–π stacking interactions are shown as red dotted lines in the figure. Each quinoline ring undergoes π–π stacking interactions with the quinoline rings of adjacent molecules on either side leading to infinite 1-D chain-like arrangements in the crystal lattice, see Fig. 2. In these interactions, the pyridine ring of the 8-HQ moiety is on top of the phenyl ring of the second 8-HQ moiety. The perpendicular distance between the rings varied between 3.491–3.5262 Å, with several C–C distances ∼3.6 Å. The rings are almost parallel (the dihedral angles between the planes vary in the range 1.7–1.77°) in an offset arrangement with slip angles β/γ (formed by the centroid–centroid vector and the ring normal) in the range 18.8–20.4°. The details of these interactions are given in Scheme S1 and Table S2, ESI.†

In addition to the π–π stacking interactions, the crystal structure of **D1** also exhibits several H-bonding and other weak bonding interactions as listed in Table 1. The solvent water molecule present in the crystal lattice also undergoes extensive H-bonding interactions. Some of these interactions such as O2–H2···O1, O3–H3···O4, O1–H1···O3, C20–H20···S1, C22–H22···S1, C12–H12···S1, C19–H19···O3, C7–H7c···S1,

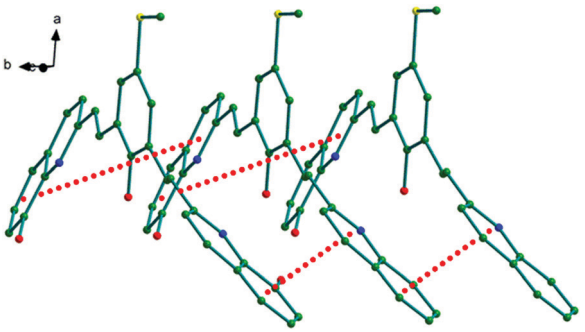

Fig. 2 Figure showing the face-to-face π–π stacking interactions (red dotted lines) among the adjacent molecules of **D1** in solid-state.

Table 1 Details of the weak bonding interactions in **D1**

D–H···A	D–H (Å)	H···A (Å)	D···A (Å)	D–H···A (°)
O2–H2···O1[1]	0.8200	2.27(6)	2.843(5)	127(6)
O3–H3···O4[2]	0.8200	1.783(6)	2.602(6)	175.7(11)
O1–H1···O3[1]	0.8200	2.40(3)	2.913(4)	121(3)
C20–H20···S1[3]	0.9300	3.086(4)	3.913(4)	149.12(7)
C27–H27···O2[4]	0.9300	2.749(6)	3.644(6)	161.94(12)
C22–H22···S1[3]	0.9300	3.212(4)	3.921(4)	134.56(8)
C12–H12···S1[5]	0.9300	3.011(5)	3.662(5)	128.41(9)
C19–H19···O3[1]	0.9300	2.986(5)	3.727(5)	137.72(10)
C7–H7c···S1[6]	0.9600	2.95(2)	3.756(5)	142(3)
O4–H4a···O3[1]	0.8500	2.08(3)	2.911(6)	166(10)
O4–H4b···O2[6]	0.8500	2.31(8)	2.962(6)	133(9)

Symmetry codes: [1]+*X*, −1 + *Y*, +*Z*; [2]+*X*, 2 + *Y*, +*Z*; [3]1 − *X*, 1/2 + *Y*, 1/2 − *Z*; [4]2 − *X*, 1 − *Y*, 1 − *Z*; [5]1 − *X*, −*Y*, 1 − *Z*; [6] +*X*, 1 + *Y*, +*Z*.

O4–H4a···O3 and O4–H4b···O2 further support and strengthen the 1-D chain-like arrangement along the crystallographic *b* axis as shown in Fig. S1 in the ESI.† Each of the 1-D chains is further connected to a similar 1-D chain through multiple C27–H27···O2 interactions in a centrosymmetric fashion as shown in Fig. S2 and S3, ESI.† The existence of strong face-to-face π–π stacking and other intermolecular interactions in the crystal lattice of **D1** points towards its potential charge transport properties as reported earlier.[12,13]

Hirshfeld surface analyses

To get quantitative and visual information about the intermolecular interactions, we calculated the Hirshfeld surfaces and the corresponding 2D-fingerprint plots for **D1** based on the single-crystal X-ray diffraction data, see Fig. 3 and 4.[20,21] Fig. 3 shows the Hirshfeld surfaces of **D1** displaying shape index and curvedness. Of these, the curvedness maps are particularly useful for identifying planar stacking arrangements.[21] Relatively large green flat regions on such surfaces indicate the possibility of stacking interactions. At the same time, the shape index surface represents fine changes in the surface shape, especially in the regions with low curvature, and highlights the regions where the two molecular Hirshfeld surfaces touch each other. The shape index mapping uses red and blue color schemes for complementary pairs of hollows and bumps. Here, the areas on the Hirshfeld surfaces that are simultaneously flat green on the curvedness map and are patterned with red and blue triangles touching each other on the shape index map are of particular importance. Such patterns, often called 'bow-tie' patterns, are characteristic of π–π stacking interactions between adjacent molecules.[22] In Fig. 3(b), one can observe such features at the

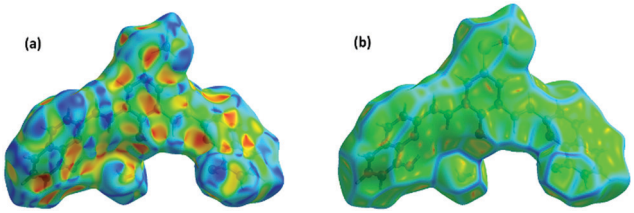

Fig. 3 Hirshfeld surfaces of **D1** mapped with (a) shape index and (b) curvedness.

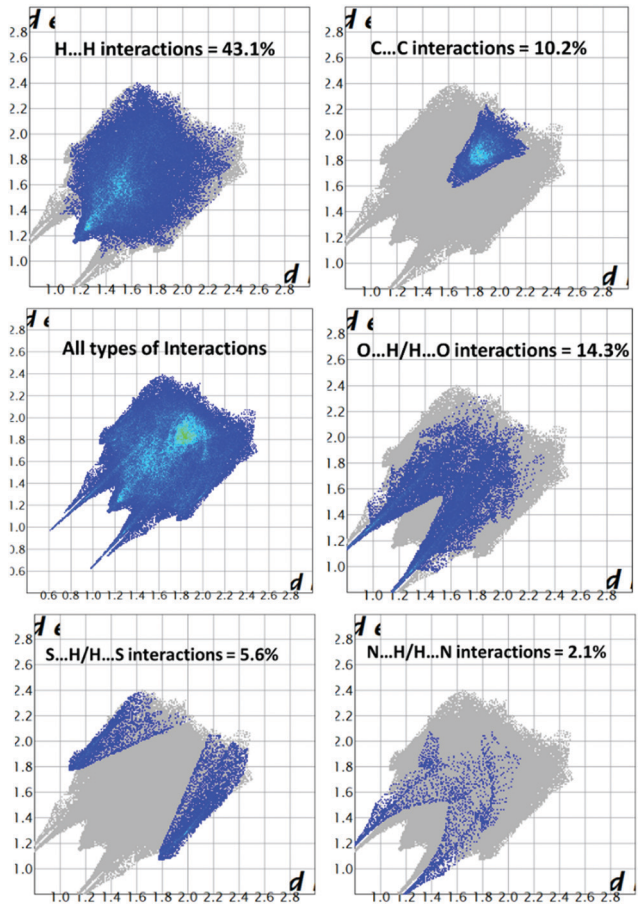

Fig. 4 2D fingerprint plots for **D1**.

flat portions of the surfaces, indicating the existence of π–π stacking interactions.

The 2D fingerprint plots of **D1** are given in Fig. 4. These plots give the percentage contribution of each contact to the total Hirshfeld surface area. As follows from these figures, the major contribution to the total Hirshfeld surface area comes from H···H, O···H and C···C contacts. The 10% contribution by the C···C contacts is substantial and further highlights the existence of π–π stacking interactions in the crystal structure. The Hirshfeld surface analyses, therefore, confirm the existence of π–π stacking interactions in the crystal structure of **D1**.

Optical and electrochemical properties

The optical and electrochemical properties of **D1** and **D2** were studied by UV-Vis absorption spectra and cyclic voltammetric analyses and the data are given in Table 2. The electronic spectra of **D1** and **D2** showed strong absorption at 402 and 398 nm respectively in tetrahydrofuran (THF) solutions (Fig. 5) and the corresponding onset absorptions were 460 and 455 nm, respectively. The optical bandgaps of **D1** and **D2** were estimated as 2.69 eV and 2.72 eV respectively, which further indicated their potential applicability as semiconducting materials.

The cyclic voltammograms of **D1** and **D2** are given in Fig. S4 (ESI†). Both **D1** and **D2** exhibited quasi-reversible oxidation waves at 0.72 V and 0.61 V ($E_{ox.}^{1/2}$, *vs.* Fc/Fc^{+}) with the corresponding onset

Table 2 The optical and electrochemical properties of **D1** and **D2**

		CV			Theoretical[a]		
Compound	λ_{abs} (nm)	HOMO (eV)	LUMO (eV)	E_g (eV)	HOMO (eV)	LUMO (eV)	E_g (eV)
D1	344, 402	−4.90	−2.21	2.69	−5.43	−2.22	3.21
D2	340, 396	−4.73	−2.00	2.72	−5.33	−1.78	3.55

[a] Simulated at the B3LYP/6-31G(d) level by Gaussian 09, details are given in ESI.

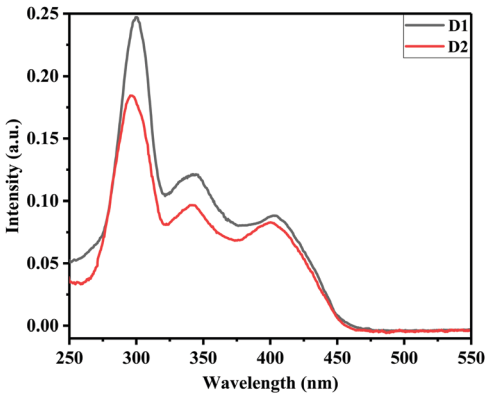

Fig. 5 Absorption spectra of **D1** and **D2** (5 μM) in THF solutions.

oxidation potentials ($E_{ox.}^{onset}$, *vs.* Fc/Fc^{+}) of 0.55 V and 0.38 V, respectively. The HOMO energies of **D1** and **D2** were estimated as −4.90 eV and −4.73 eV and the corresponding LUMO energies as −2.22 eV and −2.00 eV, respectively.[23] The HOMO energy levels exhibited by **D1** and **D2** match with the work function of silver and hence facilitate hole injection. The thermogravimetric analysis of **D1** and **D2** (see Fig. S5, ESI†) revealed their thermal stability up to 250 °C.

Performance analysis of D1 and D2 as organic semiconductors for OFET application

The semiconducting action of **D1** and **D2** was investigated by fabricating bottom-gated and top source (S)/drain (D) contact OFET structures on indium-tin-oxide (ITO) coated glass slides (Fig. 6(a)) using cost-effective spin coating technique. The ITO-coated glass slides were cleaned using hot acetone followed by isopropanol (IPA) rinsing. Thereafter, a polymethylmethacrylate (PMMA, ∼120 nm) layer was spin-coated under a controlled nitrogen environment followed by annealing at 120 °C to serve as the dielectric/insulating layer in the OFET structures as shown in Fig. 6(b). Afterward, a ∼250 nm thick active semiconducting layer was deposited by spin-coating the formulated **D1**/**D2** solutions (5×10^{-3} M in 10 ml THF; filtered with a 0.2 μm filter) at 3000 rpm (acceleration of 1500 rpm), followed by annealing at 90 °C for 15 min as shown in Fig. 6(c). OFET's source (S) and drain (D) contacts were patterned by thermal deposition of Ag through a standard shadow mask with a channel length (L) of 100 μm and channel width (W) of ∼1 mm as shown in Fig. 6(d). The electrical characteristics of the fabricated Ag/**D1**/PMMA/ITO and Ag/**D2**/PMMA/ITO OFET structures were analysed by using a Keithley 4200 SCS characterisation system.

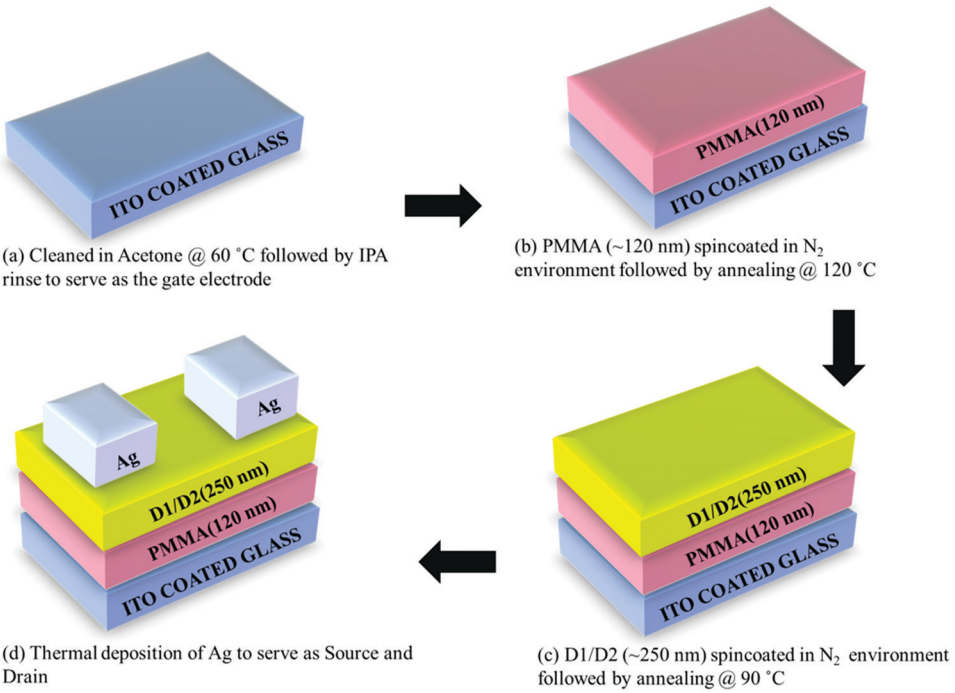

Fig. 6 Process followed for the fabrication of Ag/**D1**/PMMA/ITO and Ag/**D2**/PMMA/ITO OFET structures.

Fig. 7(a) and (b) depict the output and transfer characteristics of the fabricated Ag/**D1**/PMMA/ITO OFET structure at 75 °C. Similarly, Fig. 7(c) and (d) depict the output and transfer characteristics of the Ag/**D2**/PMMA/ITO OFET structures at the elevated temperature of 75 °C. It can be seen from Fig. 7(a) and (c) that, at a fixed negative gate to source voltage (V_{gs}), the drain (D) to source (S) current (I_{ds}) increases with increasing drain to source voltage (V_{ds}) in the negative polarity.

Since, a negative gate bias induces the accumulation of hole carriers at the interface of semiconductor and dielectric layer, the designed and developed **D1** and **D2** formulations exhibit p-type semiconducting characteristics, and Ag/**D1**/PMMA/ITO and Ag/**D2**/PMMA/ITO OFET structures were realized, thereupon. The transistor action of the fabricated bottom gate OFETs may be described by Scheme 1(c). Since the semiconductor is p-type with the majority charge carriers as holes, the channel region is formed only when the applied gate bias is <0 V as depicted in Scheme 1(c). At the applied negative gate voltage, the holes are attracted towards the interface of the semiconductor to the dielectric. Simultaneously, when the drain bias applied is also negative, *i.e.* <0 V, the accumulated holes in the channel region start to drift towards the drain (D) electrode. Here, a linear increase in the drain current (I_{ds}) with an increase in the drain voltage (V_{ds}) and a considerable saturation of the drain current as a result of an increase in the applied drain voltage establishes the transistor action of fabricated OFET structures. When the applied gate voltage is positive, *i.e.* >0 V, it can be seen that the drain current starts to decrease. These characteristics correspond to "normally open" field effect transistor. The depletion-mode FETs are normally on due to the electric field built by the existed electrons in the channel region between the source and the drain. Although these cannot be used in switching applications, this type of transistors finds their applications in discrete circuits and as startup circuits to provide some small current during the circuit's power-up sequence and to be shut-off when it is finished.[24]

When the p-type device operates in the saturation region, the standard equation is modulated to[25]

$$I_{ds\_sat} = \mu C_i \frac{W}{L}(V_{gs} - V_{th})^2, V_{ds} > (V_{gs} - V_{th}) \quad (1)$$

When it operates in the linear region, it is modulated to

$$I_{ds\_linear} = \mu C_i \frac{W}{L}\left[\{V_{gs} - V_{th}\}V_{ds} - \frac{1}{2}{V_{ds}}^2\right], \quad V_{ds} < (V_{gs} - V_{th}) \quad (2)$$

The carrier mobility was extracted from the standard MOSFET equation:[26]

$$I_{ds\_sat}^{1/2} = \mu C_i \frac{W^{1/2}}{L}(V_{gs} - V_{th}) \quad (3)$$

where μ is the field-effect mobility, L and W are the channel length and width respectively, C_i is the device capacitance per unit area, and V_{GS} and V_{th} are the gate and threshold voltages, respectively.

The computed hole mobilities of the fabricated Ag/**D1**/PMMA/ITO and Ag/**D2**/PMMA/ITO structures were $\sim$1.28 $cm^2\ V^{-1}\ s^{-1}$ and $\sim$1.10 $cm^2\ V^{-1}\ s^{-1}$ respectively at 75 °C. Parallel thereto, linear extrapolation is a standard threshold voltage (V_{th}) extraction method from MOSFETs/MISFETs transfer characteristics. Hence, the extracted threshold voltage is from the transfer characteristics (Fig. 7(b) and (d)) of Ag/**D1**/PMMA/ITO and Ag/**D2**/PMMA/ITO structures and are assessed to be around -1.55 V and -1.54 V

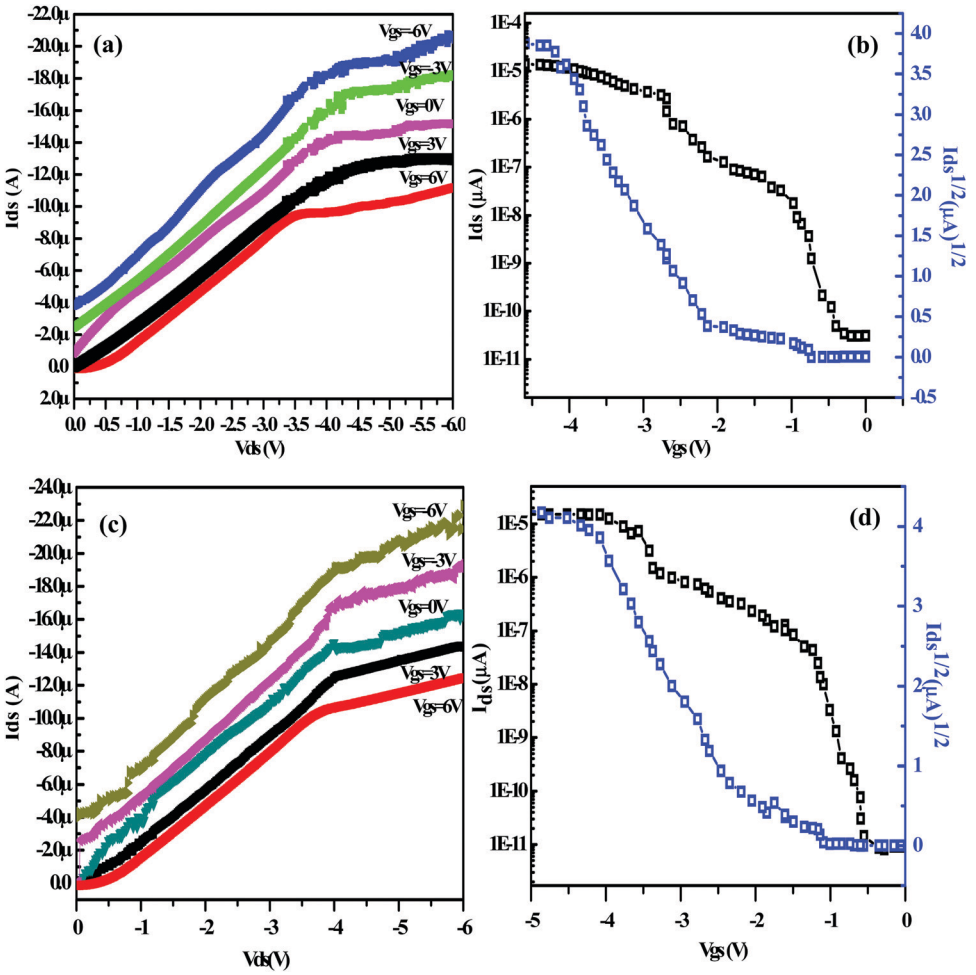

Fig. 7 Electrical characteristics of the Ag/**D1**/PMMA/ITO and Ag/**D2**/PMMA/ITO OFETs on glass substrate at 75 °C; (a) output characteristics of Ag/**D1**/PMMA/ITO, where V_{ds} was swept from 0 to −6 V at V_{gs} varied from 6 to −6 V with the step of 3 V; (b) I_{ds} *vs.* V_{gs} (logarithmic and linear scale) at V_{ds} = −6 V for gate voltage varying from −5 V to 0 V for Ag/**D1**/PMMA/ITO; (c) output characteristics of Ag/**D2**/PMMA/ITO, where V_{ds} was swept from 0 to −6 V at V_{gs} varied from 6 to −6 V with the step of 3 V; (d) I_{ds} *vs.* V_{gs} (logarithmic and linear scale) at V_{ds} = −6 V for gate voltage varying from −5 V to 0 V for Ag/**D2**/PMMA/ITO.

respectively. As listed in Table 3, it is observed that the hole mobilities of **D1** and **D2** increase upon increasing the substrate temperature from 25 to 75 °C. In comparison to **D2**, the **D1** based OFET structures exhibited higher mobilities that can reach up to ∼1.28 $cm^2\ V^{-1}\ s^{-1}$ with $I_{on/off}$ ratio up to 10^3 at 75 °C; whereas the maximum hole mobility shown by the thin films of **D2** was only up to ∼1.10 $cm^2\ V^{-1}\ s^{-1}$ (see Table 3).

The performance analyses of the OFETs based on **D1** and **D2** revealed that these semiconducting materials exhibit good hole mobilities at low voltages (<6 V). This could be attributed to the following factors.[27] A good organic semiconducting material, in principle, should have a large electron-delocalized π-conjugated system, good intermolecular interactions, and appropriate energy-level structures.[28] For higher charge mobility, the lowest unoccupied molecular orbital (LUMO) or the highest occupied molecular orbital (HOMO) of the OFETs should also favour the injection of electrons or holes. It has been noted experimentally that a HOMO level below ∼−5.0 eV and a LUMO level below ∼−3.7 eV are required for stable hole and electron transport, respectively.[29–32] As the experimentally calculated HOMO levels of **D1** and **D2** are ∼−4.90 eV and ∼−4.73 eV, they lead to stable hole injection during OFET operation.

Table 3 Hole mobility (μ), current on/off ratio (I_{on}/I_{off}), and threshold voltage (V_{th}) of OFETs with thin films of **D1** and **D2** at different substrate temperatures

	Temp. (sub.) [°C]	I_{on}/I_{off}	V_{th} [V]	μ [$cm^2\ V^{-1}\ s^{-1}$]
D1	25	9.71×10^6	−1.73	1.08
	50	4.37×10^5	−1.5	1.14966
	75	1.77×10^3	−1.55	1.276803
D2	25	5.30×10^5	−1.25	0.716413
	50	2.50×10^4	−1.41	0.85717
	75	2.37×10^4	−1.54	1.106391

For a given technology, devices are designed with a specific gate capacitance, which is directly proportional to the dielectric constant (ε_O) and inversely proportional to the thickness of the gate dielectric material (d) as per the expression:[33]

$$C_i = \frac{\varepsilon_O A}{d} \quad (4)$$

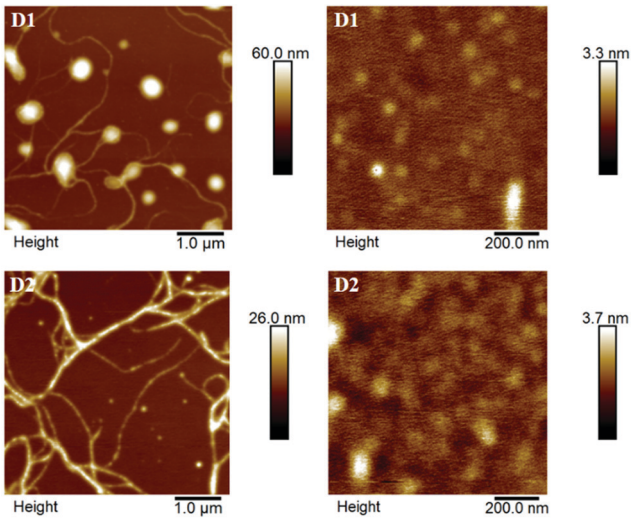

Fig. 8 Surface morphology of as deposited thin-films of **D1** and **D2** on Si substrates.

It is clear from the standard MOSFET eqn (2) that the drain current is directly proportional to the capacitance of the dielectric as stated by Michael Salinas *et al.*[33] Therefore, the low voltage operation of the fabricated devices may also be attributed to the higher dielectric constant value of PMMA (4.9)[27,34] as compared to SiO_2 (3.6). The estimated value of the effective oxide thickness of PMMA is ~95 nm, which leads to an increase in the effective device capacitance and performance of the investigated OFET structures.

There are a few reports on solution-processable p-type organic semiconductors exhibiting mobilities greater than 1.0 $cm^2\ V^{-1}\ s^{-1}$; however, many of such devices are reported to work at higher operating voltages.[35]

Between **D1** and **D2**, the OFETs based on **D1** displayed better device performance. The hole mobility exhibited by **D1** (1.08 $cm^2\ V^{-1}\ s^{-1}$) is higher than that of **D2** (0.72 $cm^2\ V^{-1}\ s^{-1}$) at room temperature. This may partly be attributed to the subtle differences in the electronic effects of –R substituent ($-SCH_3$ *vs.* $-OCH_3$) in **D1** and **D2** as reflected in their respective energy level values, see Table 2. Such subtle changes in the electronic effects of substituents are known to affect the carrier mobilities exhibited by organic semiconductor materials.[36–38] To fully understand and compare the effects of different –R groups in determining the charge transport properties, we had also attempted studies using similar compounds having different –R groups. However, those studies were unsuccessful largely due to the poor quality of the thin films obtained from such derivatives. Atomic Force Microscopy (AFM) and X-ray diffraction analyses were performed on thin films as well as powders of **D1** and **D2** to further explore the reasons behind the differences in their charge mobilities. Fig. 8 depicts the morphologies of the spin-coated thin films of **D1** and **D2** grown on SiO_2/Si as investigated using AFM. Both **D1** and **D2** exhibited large grains without significant crystalline features with an RMS surface roughness of 6.44 and 2.99 nm respectively for a 5.0 μm × 5.0 μm scan area. **D1** and **D2** exhibited ball-shaped small grains with a surface roughness of 0.26 and 0.36 nm range respectively for 1.0 μm × 1.0 μm scan area. Overall, Fig. 8 demonstrates that the films based on **D1** and **D2** exhibit good continuity and flatness required for semiconducting applications. The thin films of **D1** exhibited higher mobility which may partly be attributed to the better crystalline nature of **D1** as compared to **D2**. The better crystallinity of **D1** is also evident from the XRD data. The powder XRD data of **D1** exhibited relatively sharp peaks, while **D2** gave comparatively broader peaks showing poor crystalline nature. Both **D1** and **D2** retained this behaviour in thin films as well, see Fig. S9, ESI.† It has been noted earlier that the mobility increases when the processing induces a more extended crystallization.[39,40] This agrees with the fact that the thin films of **D2** possess relatively low hole mobility compared to **D1**.

Conclusion

In this work, we have presented two π-conjugated oligomers, 2,2′-(arylenedivinylene)bis-8-hydroxyquinolines **D1** and **D2**, bearing two vinylene-8-HQ units structured around a phenol ring. The structural, electrochemical, optical and semiconducting properties of these oligomers have been investigated. Solution-processed bottom-gate-top-contact OFET devices were fabricated using **D1** and **D2**, which revealed p-type semiconducting behaviours. The OFET structures of **D1** and **D2** exhibited good device performances with maximum hole mobilities of 1.28 $cm^2\ V^{-1}\ s^{-1}$ and current on–off ratios of 10^3 at an operating voltage below 6 V in the case of **D1**. Single crystal X-ray crystallography and Hirshfeld surface analyses of **D1** revealed a dense crystal packing with strong π–π stacking interactions among the molecules leading to infinite 1-D chain-like arrangement in the crystal lattice. The molecules are arranged in a slipped face-to-face manner with perpendicular distance between the rings varying in the range 3.491–3.5262 Å and slip angle of 18.8–20.4°. The excellent π–π stacking interactions contribute to the excellent semiconductor behaviours exhibited by this class of compounds. Even though the styryl-8-HQ derivatives are highly explored for biological and optical applications, their use as organic semiconductors is rarely documented. The present study demonstrates 2,2′-(arylenedivinylene)bis-8-hydroxyquinolines as promising solution-processable organic semiconducting materials holding potential for application in emerging electronics applications. However, more correlation studies connecting the structural and supramolecular properties of this class of compounds with their semiconducting properties are required to fully establish them as promising materials with high charge mobilities. Currently we are engaged in the development and analyses of more such examples.

Experimental section

Materials and characterization techniques

PMMA 950 A1 was obtained from Microchem, other chemicals were purchased from Sigma Aldrich. All the solvents were of spectroscopic grade and were used without further treatment. The compounds **D1** and **D2** were synthesized and characterized following a previously reported procedure.[19]

Single crystal X-ray diffraction analysis

Single-crystal X-ray data were collected on an Agilent SuperNova diffractometer, equipped with a multilayer optics monochromated dual source (Cu and Mo) and an Eos CCD detector, using Cu-Ka radiation (1.54184 Å) at room temperature. Data acquisition, reduction and absorption correction were performed by using CrysAlisPRO.[41] The structure was solved with the ShelXS[42] program using direct methods and refined on F^2 by full-matrix least-squares techniques with ShelXL[42] through the Olex^2 (v.1.2) program package.[43] Due to the poor diffracting properties of the crystal, the quality of the collected data was not very good. Because of the poor-quality data, some of the non-hydrogen atoms had to be refined isotropically. The hydrogen atoms were placed in calculated positions and refined as riding atoms using isotropic displacement parameters. The crystal and structure refinement data are summarized in Table S1, ESI.† There were a few A and B level crystallographic alerts in the Checkcif. These alerts and our explanations for the same are given in ESI.† CCDC 2065427.

For a better understanding and quantification of the intra- and intermolecular interactions present in the crystal structure of **D1**, Hirshfeld surface analyses were performed using the Crystal explorer 17.5 program.[44] The Hirshfeld surfaces were drawn from the.cif files of the compounds, with a normalized contact distance (d_{norm}), which can be expressed as a combination of internal di, external de and van der Waals (vdW) radii of the atoms as below:[22,45]

$$d_{norm} = \frac{(d_i - r_i^{vdW})}{r_i^{vdW}} + \frac{(d_e - r_e^{vdW})}{r_e^{vdW}}$$

Cyclic voltammograms were measured on a computer-controlled Autolab Electrochemical Workstation (Metrohm) instrument at room temperature; the measurements were performed in a conventional three-electrode cell using Pt as the working and counter electrodes, Ag/AgCl (saturated KCl) reference electrode, and n-Bu_4NPF_6 (0.1 M) as the supporting electrolyte at a scan rate of 50 mV s^{-1}. To calibrate the redox potentials, the cyclic voltammogram of ferrocene was measured under the same conditions. TGA-DTA measurements from room temperature to 500 °C were carried out on a Shimadzu DTG-60 instrument under dry nitrogen flow with a heating rate of 5 °C min^{-1}. The surface morphologies of the as-deposited organic semiconductors, as well as the PMMA dielectric, were examined by using atomic force microscopy (AFM; Dimension Icon from Bruker) in tapping mode with a scan rate of ~0.5 Hz at room temperature. The high aspect ratio TESPA-HAR AFM probe with resonant frequency 320–369 kHz and spring constant (k) of 20–80 N m^{-1} was used for AFM measurements. The thickness of the films was confirmed using Stylus Profilometer. The output ($I_{ds} - V_{ds}$) and the transfer characteristics ($I_{ds} - V_{gs}$) of the fabricated FETs were measured using Keithley 4200 SCS characterization system.

Author contributions

The overall experimental design and methodology were prepared by Suman Sehlangia and Prof. Chullikkattil P. Pradeep. The materials synthesis, characterization and related manuscript write-up were performed by Suman Sehlangia. The OFET device related experimental works and write-up were performed by Suman Sehlangia and Shivani Sharma under the supervision of Dr Satinder K. Sharma. Prof. Chullikkattil P. Pradeep supervised the overall project.

Conflicts of interest

There is no conflict of interest to declare.

Acknowledgements

C. P. P. thanks SERB, Govt. of India for financial support (project no. EMR/2016/002334) and AMRC, IIT Mandi for infrastructural facilities. S. S. thanks MHRD, Government of India, for a fellowship. The authors would like to thank C4DFED, IIT Mandi for providing the fabrication and characterization tools.

References

1 (*a*) Y. Qin, G. Li, T. Qi and H. Huang, *Mater. Chem. Front.*, 2020, **4**, 1554; (*b*) K. Müllen and U. Scherf, *Organic Light-Emitting Devices: Synthesis, Properties and Applications*, Wiley-VCH, 2006; (*c*) K. A. Peterson, A. Patterson, A. Vega-Flick, B. Liaob and M. L. Chabinyc, *Mater. Chem. Front.*, 2020, **4**, 3632.
2 (*a*) M. Mas-Torrent and C. Rovira, *Chem. Soc. Rev.*, 2008, **37**, 827; (*b*) J. W. Ward, Z. A. Lamport and O. D. Jurchescu, *ChemPhysChem*, 2015, **16**, 1118.
3 (*a*) Y. Huo, H.-L. Zhang and X. Zhan, *ACS Energy Lett.*, 2019, **4**, 1241; (*b*) Z. Wang, L. Zhu, Z. Shuai and Z. Wei, *Macromol. Rapid Commun.*, 2017, **38**, 1700470.
4 A. Mishra, M. K. R. Fischer and P. Bauerle, *Angew. Chem., Int. Ed.*, 2009, **48**, 2474–2499.
5 L.-H. Chou, Y. Na, C.-H. Park, M. S. Park, I. Osaka, F. S. Kim and C.-L. Liu, *Polymer*, 2020, **191**, 122208.
6 (*a*) H. Li, W. Shi, J. Song, H.-J. Jang, J. Dailey, J. Yu and H. E. Katz, *Chem. Rev.*, 2019, **119**, 3; (*b*) X. Wu, S. Mao, J. Chen and J. Huang, *Adv. Mater.*, 2018, **30**, 1705642; (*c*) L. Torsi, M. Magliulo, K. Manoli and G. Palazzo, *Chem. Soc. Rev.*, 2013, **42**, 8612.
7 (*a*) Y. Yu, Q. Ma, H. Ling, W. Li, R. Ju, L. Bian, N. Shi, Y. Qian, M. Yi, L. Xie and W. Huang, *Adv. Funct. Mater.*, 2019, **29**, 1904602; (*b*) C. Di, Y. Liu, G. U. I. Yu and D. Zhu, *Acc. Chem. Res.*, 2009, **42**, 1573; (*c*) D. J. Gundlach, *Nat. Mater.*, 2007, **6**, 173; (*d*) Y. Wen, Y. Liu, Y. Guo, G. Yu and W. Hu, *Chem. Rev.*, 2011, **111**, 3358.
8 Y.-G. Ha, *J. Nanosci. Nanotechnol.*, 2015, **15**, 6617.
9 F. Yin, L. Wang, X. Yang, M. Liu, H. Geng, Y. Liao, Q. Liao and H. Fu, *New J. Chem.*, 2020, **44**, 17552.
10 Z.-F. Yao, J.-Y. Wang and J. Pei, *Cryst. Growth Des.*, 2018, **18**, 7.
11 M. Mas-Torrent and C. Rovira, *Chem. Rev.*, 2011, **111**, 4833.
12 (*a*) X. C. Li, H. Sirringhaus, F. Garnier, A. B. Holmes, S. C. Moratti, N. Feeder, W. Clegg, S. J. Teat and R. H. Friend,

J. Am. Chem. Soc., 1998, **120**, 2206; (*b*) J. G. Laquindanum, H. E. Katz, A. J. Lovinger and A. Dodabalapur, *Adv. Mater.*, 1997, **9**, 36; (*c*) A. N. Sokolov, T. Friscic and L. R. MacGillivray, *J. Am. Chem. Soc.*, 2007, **128**, 2806; (*d*) J. E. Anthony, *Angew. Chem., Int. Ed.*, 2008, **47**, 452; (*e*) E. Ahmed, A. L. Briseno, Y. Xia and S. A. Jenekhe, *J. Am. Chem. Soc.*, 2008, **130**, 1118.

13 V. Coropceanu, J. Cornil, D. A. da Silva Filho, Y. Olivier, R. Silbey and J.-L. Bredas, *Chem. Rev.*, 2007, **107**, 926.

14 Y. Song, H. Xu, W. Chen, P. Zhan and X. Liu, *Med. Chem. Commun.*, 2015, **6**, 61.

15 M. Albrecht, M. Fiege and O. Osetska, *Coord. Chem. Rev.*, 2008, **252**, 812.

16 C. W. Tang and S. A. VanSlyke, *Appl. Phys. Lett.*, 1987, **51**, 913.

17 F. Liang, J. Chen, Y. Cheng, L. Wang, D. Ma, X. Jing and F. Wang, *J. Mater. Chem.*, 2003, **13**, 1392.

18 H.-P. Zeng, X.-H. OuYang, T.-T. Wang, G.-Z. Yuan, G.-H. Zhang and X. Zhang, *Cryst. Growth Des.*, 2006, **6**, 1697.

19 S. Sehlangia, M. Devi, N. Nayak, N. Garg, A. Dhir and C. P. Pradeep, *ChemistrySelect*, 2020, **5**, 5429.

20 M. A. Spackman and P. G. Byrom, *Chem. Phys. Lett.*, 1997, **267**, 215.

21 J. J. McKinnon, M. A. Spackman and A. S. Mitchell, *Acta Crystallogr., Sect. B: Struct. Sci.*, 2004, **60**, 627.

22 (*a*) J. McKinnon, M. Spackman and A. Mitchell, *Acta Crystallogr., Sect. B: Struct. Sci.*, 2004, **60**, 627; (*b*) A. Y. Sosorev, V. A. Trukhanov, D. R. Maslennikov, O. V. Borshchev, R. A. Polyakov, M. S. Skorotetcky, N. M. Surin, M. S. Kazantsev, D. I. Dominskiy, V. A. Tafeenko, S. A. Ponomarenko and D. Y. Paraschuk, *ACS Appl. Mater. Interfaces*, 2020, **12**, 9507.

23 (*a*) J. Pommerehene, H. Vestweber, W. Guss, R. F. Mahrt, H. Bassler, M. Prorsch and J. Daub, *J. Adv. Mater.*, 1995, **7**, 551; (*b*) H. Xin, J. Li, C. Ge, X. Yang, T. Xuea and X. Gao, *Mater. Chem. Front.*, 2018, **2**, 975.

24 S.-M. Kang and Y. Leblebigi, *CMOS Digital Integrated Circuits*, New York, 3rd edn, 1998.

25 S. Sharma, R. Khosla, S. Das, H. Shrimali and S. K. Sharma, *Org. Electron.*, 2018, **57**, 14.

26 S. Sharma, R. Khosla, S. Das, H. Shrimali and S. K. Sharma, *IEEE Trans. Electron Devices*, 2019, **66**, 3236.

27 (*a*) A. Y. Amin, A. Khassanov, K. Reuter, T. Meyer-Friedrichsen and M. Halik, *J. Am. Chem. Soc.*, 2012, **134**, 16548; (*b*) D. Ji, X. Xu, L. Jiang, S. Amirjalayer, L. Jiang, Y. Zhen, Y. Zou, Y. Yao, H. Dong, J. Yu, H. Fuchs and W. Hu, *J. Am. Chem. Soc.*, 2017, **139**, 2734.

28 C. Lu, Z. Ji, G. Xu, W. Wang, L. Wang, Z. Han, L. Li and M. Liu, *Sci. Bull.*, 2016, **61**, 1081.

29 C. Guo, J. Quinn, B. Sun and Y. Li, *Polym. Chem.*, 2015, **6**, 6998.

30 D. M. de Leeuw, M. M. J. Simenon, A. R. Brown and R. E. F. Einerhand, *Synth. Met.*, 1997, **87**, 53.

31 B. S. Ong, Y. Wu, P. Liu and S. Gardner, *J. Am. Chem. Soc.*, 2004, **126**, 3378.

32 A. Facchetti, *Chem. Mater.*, 2011, **23**, 733.

33 M. Salinas, C. M. Jager, A. Y. Amin, P. O. Dral, T. Meyer-Friedrichsen, A. Hirsch, T. Clark and M. Halik, *J. Am. Chem. Soc.*, 2012, **134**, 12648.

34 M. S. Tamboli, P. K. Palei, S. S. Patil, M. V. Kulkarni, N. N. Maldar and B. B. Kale, *Dalton Trans.*, 2014, **43**, 13232.

35 (*a*) H. Ju, K. Wang, J. Zhang, H. Geng, Z. Liu, G. Zhang, Y. Zhao and D. Zhang, *Chem. Mater.*, 2017, **29**, 3580; (*b*) F. Yin, L. Wang, X. Yang, M. Liu, H. Geng, Y. Liao, Q. Liao and H. Fu, *New J. Chem.*, 2020, **44**, 17552; (*c*) A. Anjali, R. Dheepika, P. M. Imran, N. S. P. Bhuvanesh and S. Nagarajan, *ACS Appl. Electron. Mater*, 2020, **2**, 2651; (*d*) T.-R. Chen, *Mater. Lett.*, 2005, **59**, 1050; (*e*) L. Yang, N. Zhang, Y. Han, Y. Zou, Y. Qiao, D. Chang, Y. Zhao, X. Lu, J. Wu and Y. Liu, *Chem. Commun.*, 2020, **56**, 9990.

36 M. R. Niazi, E. Hamzehpoor, P. Ghamari, I. F. Perepichka and D. F. Perepichka, *Chem. Commun.*, 2020, **56**, 6432.

37 S. J. Cho, M. J. Kim, Z. Wu, J. H. Son, S. Y. Jeong, S. Lee, J. Ho Cho and H. Y. Woo, *ACS Appl. Mater. Interfaces*, 2020, **12**, 41842.

38 C.-H. Kuo, D.-C. Huang, W.-T. Peng, K. Goto, I. Chao and Y.-T. Tao, *J. Mater. Chem. C*, 2014, **2**, 3928.

39 (*a*) C. H. Woo, C. Piliego, T. W. Holcombe, M. F. Toney and J. M. J. Frechet, *Macromolecules*, 2012, **45**, 3057; (*b*) J. F. Chang, B. Q. Sun, D. W. Breiby, M. M. Nielsen, T. I. Solling, M. Giles, I. McCulloch and H. Sirringhaus, *Chem. Mater.*, 2004, **16**, 4772.

40 R. D. Pietro, T. Erdmann, J. H. Carpenter, N. Wang, R. R. Shivhare, P. Formanek, C. Heintze, B. Voit, D. Neher, H. Ade and A. Kiriy, *Chem. Mater.*, 2017, **29**, 10220.

41 CrysAlisPro Program, version 171.37.33c, Agilent Technologies, Oxford, UK, 2012.

42 G. M. Sheldrick, *Acta Crystallogr., Sect. A: Found. Crystallogr.*, 2008, **64**, 112.

43 O. V. Dolomanov, L. J. Bourhis, R. J. Gildea, J. A. K. Howard and H. J. Puschmann, *J. Appl. Crystallogr.*, 2009, **42**, 339.

44 M. A. Spackman and J. J. McKinnon, *CrystEngComm*, 2002, **4**, 378.

45 B. Kupcewicz and M. Malecka, *Cryst. Growth Des.*, 2015, **15**, 3893.